IEEE Access
Multidisciplinary | Rapid Review | Open Access Journal

Received 14 April 2024, accepted 12 May 2024, date of publication 16 May 2024, date of current version 24 May 2024.

Digital Object Identifier 10.1109/ACCESS.2024.3401865

RESEARCH ARTICLE

Design and Analysis of a Low Profile Millimeter-Wave Band Vivaldi MIMO Antenna for Wearable WBAN Applications

JAWAD AHMAD[1], (Student Member, IEEE), MOHAMMAD HASHMI[1], (Senior Member, IEEE), AZAMAT BAKYTBEKOV[1], AND FRANCISCO FALCONE[2], (Senior Member, IEEE)

[1]Department of Electrical and Computer Engineering, School of Engineering and Digital Sciences, Nazarbayev University, 010000 Astana, Kazakhstan
[2]Institute of Smart Cities, Public University of Navarre, 31006 Pamplona, Spain

Corresponding author: Mohammad Hashmi (mohammad.hashmi@nu.edu.kz)

This work was supported in part by Nazarbayev University under Grant 20122022FD4113 and Grant 201223FD2601.

ABSTRACT The development of a reliable Wireless Body Area Network (WBAN) relies significantly on the quality of wearable antennas. Therefore, this paper proposes a low-profile four-element Multi-Input-Multi-Output (MIMO) antenna for wearable millimeter-wave (mm-wave) WBAN applications. The MIMO antenna structure incorporates a standard Vivaldi antenna and a frequency-selective surface that encompasses the 28 GHz and 30 GHz of the mm-wave band with a 36.44% fractional bandwidth. It offers inter-element isolation of less than −20 dB in a compact space of $16 \times 20\ mm^2$. Conformability analysis, along with testing on Gustav's model chest, hand, and leg, was evaluated in terms of the antenna impedance bandwidth, gain, efficiency, and radiation pattern. The simulated characteristics of the MIMO antenna were tested through measurements in free space and on the human body using a prototype of the antenna. Furthermore, the MIMO antenna exhibits a low envelope correlation coefficient of less than 0.24, high diversity gain of greater than 9.95 dB, and an acceptable total active reflection coefficient of less than −10 dB. To ensure safety, the Specific Absorption Rate (SAR) analysis revealed acceptable levels of 0.397 and 0.267 (W/kg) at 28 GHz and 30 GHz, respectively. The proposed MIMO design is suitable for wearable WBAN applications owing to its small size, consistent gain, and compatibility with the human body in terms of a constant impedance bandwidth and end-fire radiation pattern.

INDEX TERMS Antenna, MIMO antenna, on-body antenna, Vivaldi, wireless body area network (WBAN).

I. INTRODUCTION

The rapid advancement of wearable devices and gadgets for Wireless Body Area Networks (WBANs) has recently garnered considerable interest from researchers [1]. The COVID-19 pandemic has prompted healthcare professionals to recognize the expansion of contactless medical operations as a preventive measure against future outbreaks. In addition, owing to the increase in the aging population, healthcare providers are actively exploring strategies to outsource medical services in order to address the increased workload. This presents a valuable opportunity to adopt WBAN in the field of medical care [2], [3]. A WBAN comprises wearable computing devices that can be implanted within the body, attached to the body, or carried in various ways, such as clothing pockets or bags. The expansion of physiological sensors, low-power integrated circuits, and wireless communication has led to the development of a new generation of wireless sensor networks, which are now employed for various purposes, including health monitoring, traffic management, crop surveillance, and infrastructure assessment [4].

The associate editor coordinating the review of this manuscript and approving it for publication was Wanchen Yang.

WBAN technology relies on antennas for communication and requires miniaturization. This is due to the requirement for antenna systems to be both low-profile and efficient to fit within the limited space available in a WBAN [5]. Selection of antenna type and multiband or wideband support is important for guaranteeing an uninterrupted wireless connection [6]. Similarly, such antennas must be sufficiently flexible to fit curved body parts. Elastomeric PDMS [7], conductive fabrics [8], and fractal-like structures [9] have been used to fabricate antennas with improved body mobility. However, limitations such as durability, sensitivity to environmental factors, complex tuning, and soldering issues in wearable antennas must be addressed [10], [11], [12]. An all-textile multiband microstrip circular patch antenna with a low profile was proposed for WBAN applications [13]. The antenna is suitable for low-frequency wearable applications owing to the denim-integrated conductive fabric layer, which makes it extremely low-profile. In [14], on-body measurements were conducted on a human body in various regions, such as the chest, back, arm, and leg, to evaluate the performance of a patch antenna for WBAN applications. The results demonstrated stable radiation patterns and good impedance-matching characteristics. Additionally, [15] presented a discussion of a compact microstrip-based textile antenna with a full ground plane that operates in the frequency range of 3.1–10.6 GHz. The antenna was fabricated using a low-cost FR4 substrate and copper tape. The performance and influence of a one-turn circular patch antenna array on the human body have been studied [16]. The study revealed a stable radiation pattern and commendable impedance-matching characteristics for the antenna while highlighting the human body has a significant impact on performance. In [17], an antenna was fabricated using a flexible substrate and copper tape, resulting in a wide bandwidth of 100 MHz and a stable radiation pattern. Despite their compact size, ease of fabrication, and low weight, these antennas have limited bandwidth, which hinders the simultaneous transmission of multiple forms of data, such as biological and communication data.

Challenges exist in the development of wearable antennas that emit minimal radiation into the human body. Owing to their proximity to the body, wearable antennas must be designed to minimize the amount of radiation absorbed by the human body while maintaining their functionality. Ensuring that the Specific Absorption Rate (SAR) stays within safe limits (SAR < 1.6 W/kg (Federal Communication Commission (FCC) standard) and < 2 W/kg (European Union (EU) standard)) is crucial to prevent potential health risks. Some studies have suggested using a metamaterial bandgap and artificial magnetic conductor (AMC) layers placed at the back of the antenna to address the issue of heat absorption by the human body [18], [19], [20], [21]. However, this approach has challenges as it can add extra thickness and a quarter wavelength spacing between the antenna element and the AMC layer, which can make it difficult to incorporate antenna elements with other devices into a single wearable device platform [22]. As an alternative, tapered slot antennas (i.e., Vivaldi antennas) offer a wide bandwidth and directional end-fire radiation patterns. Using such antennas, the need for additional metamaterial-backed layers in WBAN antenna systems can be significantly reduced because of their end-fire radiation, which lies parallel to the human body. Although a few studies have utilized end-fire antennas designed specifically for WBANs to operate within the 2.4 GHz ISM band and UWB [23], [24], [25], these frequency bands are becoming congested owing to the increasing use of electronic gadgets. As a result, using higher frequency bands, such as the millimeter wave (mm-wave) band, has been proposed.

The utilization of mm-wave frequencies within WBANs can facilitate rapid medical data transfer due to their high data rates and extensive bandwidth availability. Moreover, these frequencies can enhance privacy and security because of their shorter wavelengths and limited transmission range, thereby reducing the risk of unauthorized access and data interception [26]. Despite the substantial advantages of the mm-wave band and tapered slot antennas in WBANs, relatively few studies have been conducted to explore their potential. One study reported a Yagi-Uda antenna that has a broad frequency range of 57-64 GHz and a gain of 12 dBi [27], although its practical feasibility may be hampered by its substantial dimensions (8× 28 mm). Another study discussed a helical-inspired antenna that was tested for end-fire radiation patterns at 28 GHz [28]. A few wearable end-fire textile antennas have been proposed for on-body [29] and off-body communication [30] at 60 GHz, achieving radiation efficiency less than 50%. In [31], a reflector-backed antenna was proposed for WBAN energy harvesting, which resulted in an approximate 67% radiation efficiency.

Single-antenna elements are commonly used for communication in wearable devices owing to their low profile and ease of integration. However, the use of a single element has certain limitations. Single-antenna systems are prone to experiencing multi-path fading and obstructions caused by the human body, which can result in reduced performance. Incorporating multi-input-multi-output (MIMO) antennas in WBANs can mitigate the impacts of signal fading and multipath interference caused by body movements and obstructions [32], [33]. In addition, MIMO antennas can provide increased spatial diversity and multiplexing, leading to improved coverage, data rates, and power efficiency [34]. However, designing compact MIMO antennas can be challenging because of the proximity of their elements, which can result in high mutual coupling. To address this issue, various techniques have been employed to reduce mutual coupling [35], [36], [37]. Nevertheless, these techniques are inadequate for on-body WBAN antennas owing to their multi-layer decoupling structures and susceptibility to bending and interference. Therefore, to address these limitations, this work presents a highly compact and efficient four-port Vivaldi MIMO antenna for the mm-wave band

WBAN. The main contributions of this study can be summarized as follows:

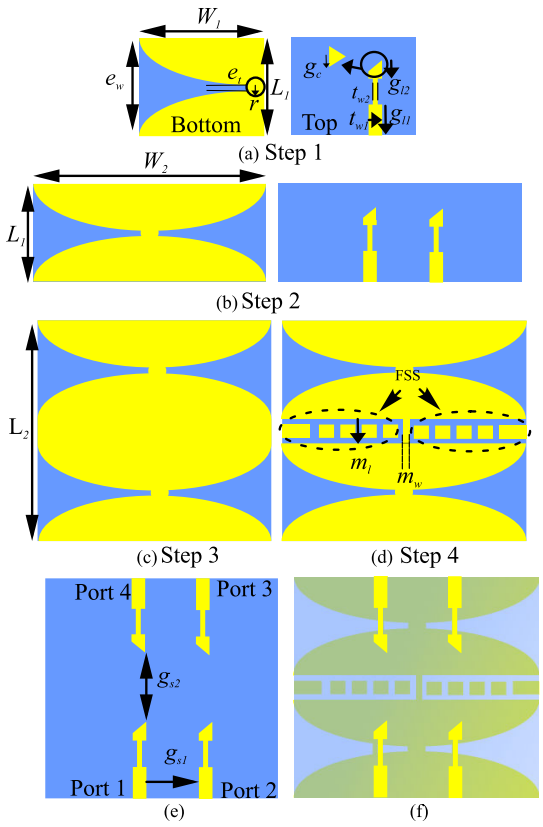

FIGURE 1. Proposed MIMO antenna design steps (a) single element (b) two elements (c) four elements without FSS (d) proposed final four elements with FSS (e) inter-element spacing, and (f) perspective view of the design.

1) Wide bandwidth availability: MIMO antenna with a tapered slot design and small footprint physical area. The antenna covers 24.25 − 27.50 GHz n257 and 26.50 − 30 GHz n258 5G bands.
2) Less isolation: The implementation of frequency-selective surfaces (FSS) between the antenna elements enhances inter-element isolation to more than −20 dB in simulations and measurements.
3) Less prone to bending: Bending analysis demonstrates that the antenna's symmetrical structure minimally affects performance.
4) Gain and efficiency: A compact design that exhibits constant gain and efficiency throughout the impedance bandwidth.
5) Safety: An evaluation of the proposed design in the mm-wave spectrum for biocompatibility in terms of SAR according to the guidelines outlined in IEEE C95.1-1999 for 1 g of tissue demonstrates that the SAR of the antenna is below the acceptable standards, which suggests that it is biocompatible.
6) Improved Spatial Coverage: The utilization of antennas transmitting radio signals in opposite directions generates a wider coverage area surrounding the body, which in turn decreases the probability of signal obstructions or weakening resulting from the human body. This is especially important for WBAN applications, where dependable and uninterrupted communication between body-worn sensors and a central hub is of paramount importance.
7) Reduced Power Consumption: With capacity to cover a larger area with the same signal strength, the necessity for high transmission power from each antenna is minimized. This can result in reduced energy consumption for the overall WBAN system, which is crucial for wearable devices powered by batteries, as extending battery life is a significant concern.

TABLE 1. Parameters of the MIMO antenna and FSS structure.

Parameters	Values (mm)	Parameters	Values (mm)	Parameters	Values (mm)
W_1	10.00	W_2	20.00	L_1	7.00
L_2	16.00	e_t	0.41	r	0.71
g_{l1}	2.70	g_{l2}	1.00	t_{w1}	0.65
t_{w2}	0.20	g_c	0.61	m_l	2.00
m_w	0.30	g_{s1}	6.35	g_{s2}	6.10
f_{l1}	1.05	f_{l2}	1.50	f_s	1.08
F_w	1.30	F_{sl}	10.50		

The sensors used in WBAN involve two communication methods: on-body and off-body communication. On-body communication is utilized for communication between sensor nodes within the body, whereas off-body communication is used to send information to external nodes. A promising solution involves the use of a single antenna for both methods. This strategy simplifies the design and provides a balance between comfort, performance, and ease of use. The integration of the proposed MIMO Vivaldi antenna on a single substrate within the sensor nodes can create a compact and efficient system. This approach can offer several benefits, including a reduction in the size of the wearable device, efficient signal transmission for both on-body and off-body communication channels, and streamlined fabrication processes that can reduce production costs and improve device reliability.

The remainder of this paper is organized as follows. Section II discusses the geometrical design and layout of the MIMO antenna and a decoupling technique for isolation enhancement. Section III analyzes the results and discussion, particularly the results of conformability, on-body performance, the impact of fabric thickness, and measurements of a fabricated prototype. Section IV reports the calculation of MIMO antenna diversity parameters. A safety analysis in terms of SAR values is presented in Section V, the comparison of proposed design with other works is reported in section VI, and Section VII concludes the study.

II. MIMO ANTENNA DESIGN AND ANALYSIS

The MIMO antenna design process consists of several stages that are outlined in subsequent subsections. The design process began with a basic single-element configuration and progressed to incorporate two and four elements, as depicted in Fig. 1. To suppress mutual coupling and improve the isolation between the elements of the antenna, a decoupling structure was eventually added. The addition of multi-ports in an antenna allows it to take advantage of spatial diversity, which is critical in WBAN scenarios where the on- and off-body environment can result in significant signal fading due to multipath propagation and changes in user posture. This MIMO antenna design, which integrates multiple highly isolated radiating elements, can potentially enhance overall signal reception/transmission and establish more reliable connections. The optimized parameters and values of the MIMO antenna are provided in Table 1.

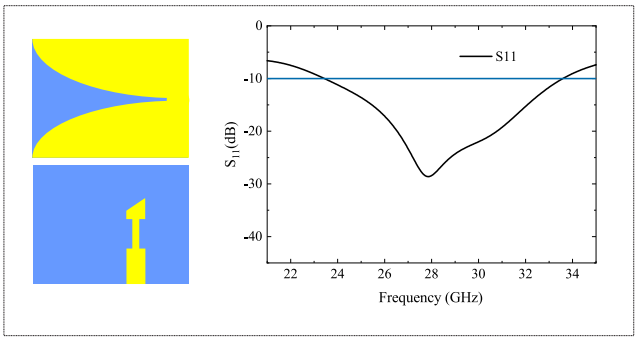

FIGURE 2. Reflection coefficient of the step 1 (single element) antenna.

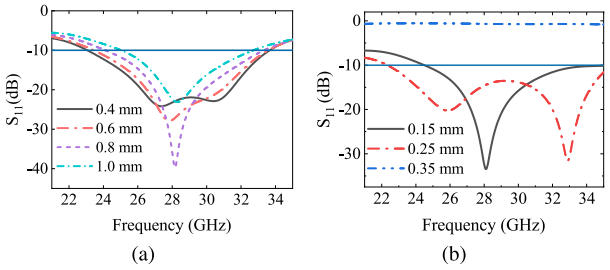

FIGURE 3. Parametric analysis of variables g_c and t_{w2}.

A. SINGLE ELEMENT DESIGN

The design of the single-port Vivaldi antenna is fabricated on a semi-flexible Rogers RT5880 substrate having permittivity of 2.2 and loss tangent of 0.0009 as depicted in Fig. 1(a). The substrate's thickness was 0.79 mm, while the copper metal's thickness was 0.017 mm. In this configuration, the Vivaldi tapering slot functions as a defected ground structure, which assist the reduction in the size of the antenna. Initially, two radiating flares were designed, which was then joined by a circle with a radius r. It is essential to recognize that the radius significantly influences the resonant behavior of the antenna. The antenna is fed by electromagnetic coupling between the microstrip and the slot line. The total length of the microstrip line on the top face measures 4.95 mm, and its width has been divided into two parts, t_{w1} and t_{w2}, to achieve the required impedance bandwidth. The performance of the antenna was also enhanced through a triangular cut g_c on the top of the microstrip line. The tapering slot configuration on the bottom face was designed by utilizing equations (1)-(3) [38].

$$y = c_1 e^{rx} + c_2 \tag{1}$$

where c_1 and c_2 are determined by the opening rate r and the two points p_1 (x_1, y_1) and p_2 (x_2, y_2).

$$c_1 = \frac{y_2 - y_1}{e^{rx_2} - e^{rx_1}} \tag{2}$$

$$c_2 = \frac{y_1 e^{rx_2} - y_2 e^{rx_1}}{e^{rx_2} - e^{rx_1}} \tag{3}$$

The exponential tapered curve has a minimum point at p_1, located at (x_1, y_1), and a maximum point at p_2, located at (x_2, y_2). Using the values of y_1 and y_2, the cut-off frequencies of the Vivaldi antenna can be determined through the aperture width e_w expressed in (4). The opening rate, denoted by r, is the exponential factor that determines the Vivaldi antenna beamwidth, whereas c_1 and c_2 are constants.

$$e_w = \frac{c}{f_{min}\sqrt{\epsilon_r}} \tag{4}$$

Here, c represents the speed of light, and ϵ_r signifies the dielectric constant of the material. Any changes to these values will lead to alterations in the antenna and its characteristics. The simulated reflection coefficient of the single-element antenna is given in Fig. 2. The single-element antenna design spans an impedance bandwidth of over 10 GHz, ranging from 23.45 GHz to 33.59 GHz. Initially, the microstrip line was employed without any cuts, but its bandwidth was outside the desired region. Consequently, parametric analyses were conducted on the variables g_c and t_{w2} and the results are provided in Fig. 3. It is evident that the bandwidth is significantly impacted by variations in these parameters. For instance, the bandwidth is considerably reduced when the variable g_c is increased from 0.4 mm to 1.0 mm. Additionally, almost full reflection was observed when the variable t_{w2} was increased to 0.35 mm and beyond.

B. MULTI-ELEMENT DESIGN

As illustrated in Fig. 4(a), the two-element design is the mirror of the single-element design which is directed in opposite directions. The impedance bandwidth of this configuration is also more than 10 GHz, spanning from 23.45 GHz to 33.56 GHz, as shown in Fig 4(a). Despite the close spacing of the ports, the antenna element configurations in opposite directions exhibited good isolation (> -20 dB). This is due to the Vivaldi antenna's design, which is characterized by a tapered shape that helps minimize interference. As the width of the antenna elements increases toward the radiating end, the currents flowing on the surface of the antenna tend to concentrate at the edges. By orienting the antennas

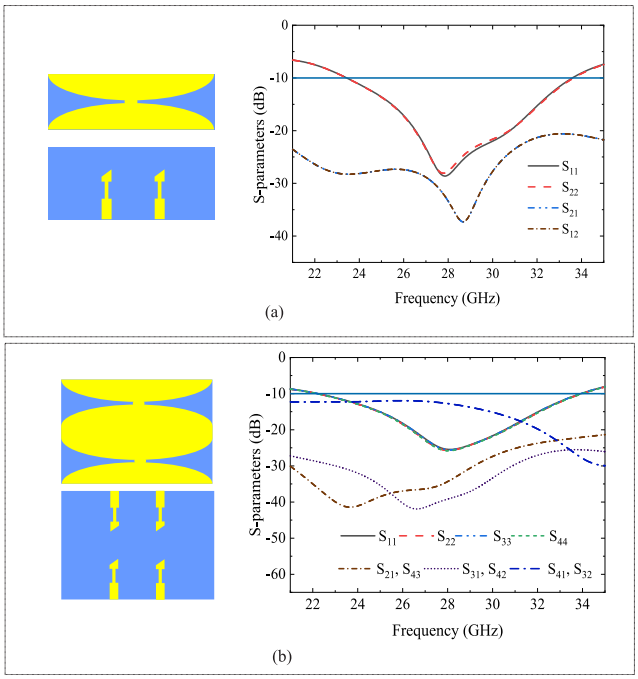

FIGURE 4. Multi-element antenna design: (a) reflection and transmission coefficients of step 2, and (b) reflection and transmission coefficients of step 3.

in different directions, the edge currents experience less interaction, which in turn reduces unwanted coupling even further.

In order to construct a four-element antenna, the designed MIMO antenna was mirrored in the vertical direction, resulting in a structure where two of the elements radiate in the same direction while the others radiate in different directions as shown in Fig. 4(b). The utilization of a multi-port design slightly increased the impedance bandwidth having an impedance bandwidth range of 22.97 GHz to 33.91 GHz, respectively. Consequently, the MIMO design achieved a fractional bandwidth of approximately 38.46%. A considerable high level of isolation can be observed between antenna components that transmit in opposing directions, particularly S_{21}, S_{43}, S_{31}, and S_{42}. It is worth noting that this isolation is more pronounced (> -14 dB) when the components transmit in the same direction. This is evident due to the tapering structure that is in close proximity to each other, which results in the distribution of current from one antenna disrupting the other. This can lead to interference, reduced data rates, and degraded system performances. The proper placement of the feeding ports is essential to guarantee adequate separation between them, which in turn reduces unwanted coupling that could negatively impact the antenna's radiation pattern. This design considers a spacing of 6.35 mm between ports, which is approximately half the wavelength of the lower resonant frequency at 24 GHz.

The isolation can be enhanced either by increasing the spacing between input ports of the MIMO antenna or by using some isolation enhancement techniques such as defective ground structure (DGS) or using metamaterials based FSS. Although increasing the spacing between antenna input ports improves isolation, it can also affect the dimensions of the antenna, which may not be ideal for compact and efficient components in WBAN. In this regard, a negative permeability-based FSS structure was utilized in this work to achieve a high isolation level while maintaining the compactness of the design.

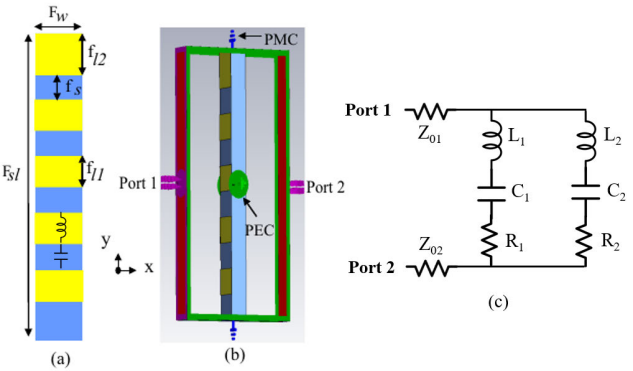

FIGURE 5. FSS design: (a) structure, (b) boundary conditions, and (c) equivalent circuit model.

C. ISOLATION ENHANCEMENT TECHNIQUE

FSS can have negative effective permeability and permittivity values at different frequencies and works as filters. The wave-number 'k' of such materials is imaginary with respect to the natural electromagnetic media. Materials that exhibit negative permeability or permittivity are referred to as single-negative (SNG) metamaterials. When passing through an SNG metamaterial, electromagnetic (EM) waves undergo high levels of evanescence. For instance, the excitation of antenna 1 induces a current on nearby antennas through a strong electric field x-component, causing inter-element mutual coupling. When an FSS with negative permeability is placed between antenna elements, it creates a region with negative permeability and positive permittivity ($\mu_r < 0, \varepsilon_r > 0$) [39]. Within this region, the k can be expressed as:

$$k = k_0 \cdot \sqrt{-|\mu_r| \cdot |\varepsilon_r|} = jk_0 \cdot \sqrt{|\mu_r| \cdot |\varepsilon_r|} \tag{5}$$

Under this condition, the corresponding x-component of the electric field ($A_0 \cdot e^{jkx}$) traveling along the negative x-direction can be expressed as follows:

$$A_0 \cdot e^{jkx} \cdot e^{j\omega t} = A_0 e^{(-k_0 \cdot \sqrt{|\mu_r| \cdot |\varepsilon_r|})} \cdot e^{j\omega t} \tag{6}$$

where the electric field amplitude is A_0 and ω is the angular frequency. Eq. (6) shows that the EM waves traveling along the negative x-direction of the FSS surface are evanescent. When the wave radiated by the antennas propagates along the Z-direction, the magnetic field component is oriented in the x-direction, leading to effective radiation owing to the anisotropic nature of the FSS.

D. FSS AND FINAL MIMO DESIGN

The performance of Vivaldi antennas can be significantly affected by the sensitivity of the radiation flares or tapering structures to slots [40]. To mitigate these effects and enhance the inter element isolation, the FSS structure is designed with a narrow width that does not significantly impact the tapering structures. The proposed design consists of five rectangle-shaped patches separated by a distance f_s, as depicted in Fig. 5(a). While various conventional FSS topologies, including hexagonal, circular, and fractal shapes exist, the choice of a rectangle-shaped FSS offers both modeling simplicity and enhanced performance, particularly in terms of stability to the incident angles. As the FSS is used in the MIMO antenna, the Rogers RT5880 substrate and copper metal patches with the same thickness were utilized in the FSS design.

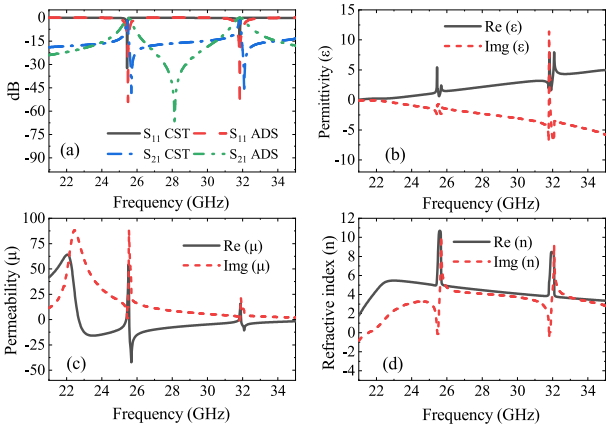

FIGURE 6. FSS unit cell: (a) S-parameters (b) permittivity (c) permeability, and (d) refractive index.

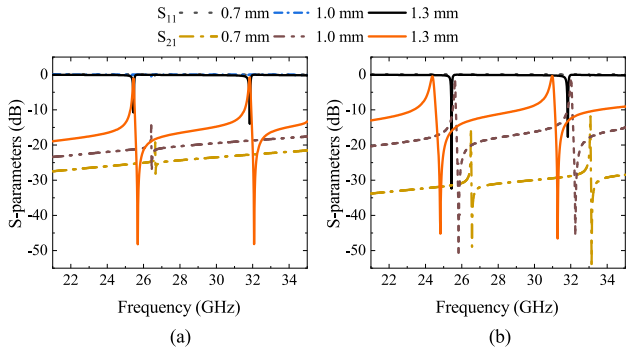

FIGURE 7. Parametric analysis of the FSS: (a) reflection and transmission coefficients due to separation (f_s) between patches, and (b) reflection and transmission coefficients due to width of the patch (F_W).

The FSS was simulated using perfect magnetic (PMC) and perfect electric (PEC) boundary conditions in CST, as shown in Fig. 5(b). The FSS structure displays a reflection coefficient of nearly 0 dB and a transmission coefficient of over -18 dB across most of the bandwidth, resulting in band-stop characteristics as shown in Fig. 6(a). Although the FSS demonstrates two band-pass frequencies of 25.82 GHz and 31.93 GHz, they are notably distant from the desired 28 GHz and 30 GHz frequencies. Moreover, such FSS structures can be modeled as parallel inductive (L) and capacitive (C) circuits. The FSS design encompasses a multitude of patches, which can be viewed as individual L and C components that operate concurrently. In this context, L denotes the inductance of the patches, while C signifies the distance between them. As the conductor has minimum small resistance, thus the patch resistance can be modeled as R, resulting in the overall circuit representation of the FSS structure as shown in Fig. 5(c), where Z_{01} and Z_{02} are the characteristics impedance of free space. The optimized values of RLC equivalent circuit model are as follows: $L_1 = 300$ nH, $L_2 = 192.30$ nH, $C_1 = C_2 = 0.00013$ pF, $R_1 = R_2 = 1$ mΩ, and $Z_{01} = Z_{02} = 377\Omega$. The ADS schematic environment was utilized to simulate the RLC equivalent circuit model, and the results were compared with the CST simulation, as depicted in Fig. 6(a). The findings confirm a satisfactory approximation of the equivalent circuit by the electromagnetic simulated CST model.

The Kramers-Kronig relationship was applied to calculate the effective permittivity, permeability, and refractive index of the FSS configuration [41]. The FSS unit cell exhibits negative effective permeability across a significant portion of the impedance bandwidth, while both permittivity and refractive index remain positive and are depicted in Figs. 6(b)-(d). Additionally, a parametric analysis was conducted to investigate the impact of patch width and separation on the reflection and transmission characteristics of the proposed unit cell, as shown in Fig. 7(a) and Fig. 7(b). The results indicate that increasing the separation and width of the patches affects the resonance frequency, causing it to shift towards the left side of the frequency band. When the distance between the two patches was less than 0.7 mm, a high level of reflection was observed; however, the resonant frequency was not within the desired frequency range. Moreover, an increase in the width of the patches resulted in an elevated transmission coefficient. Therefore, it is crucial to carefully consider the values of these parameters when selecting the proposed FSS unit cell design. Table 1 presents the optimized dimensions of the FSS unit cell.

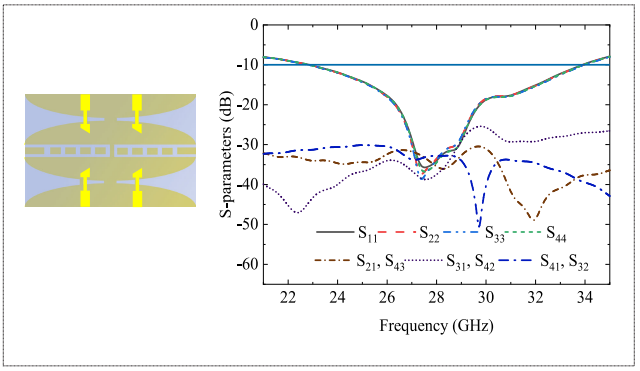

FIGURE 8. Reflection and transmission coefficients of the step 4 (final design) of the MIMO antenna.

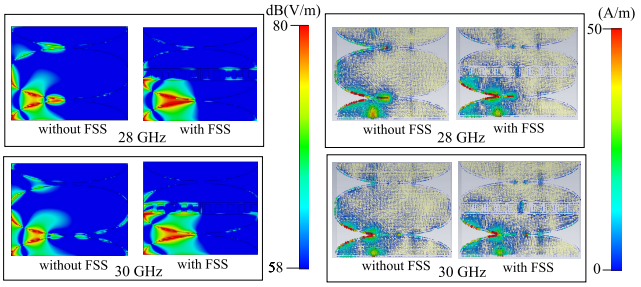

FIGURE 9. Electric field (left) and surface current (right) distribution with and without FSS on the ground plane.

A slot was created and the FSS meta-unit cells were embedded into the ground of the MIMO antenna to improve the isolation level. The incorporation of the FSS structure has only a negligible impact on the impedance bandwidth, whereas the isolation level of certain antennas is enhanced, specifically between antennas 1 and 4, and antennas 2 and 3, as shown in Fig. 8. For instance, the isolation level between antennas 1 and 4 was significantly higher (−14 dB) without the FSS structure. However, with the inclusion of the FSS structure, the isolation between ports 1 and 4 improved to greater than −31 dB across the majority of the impedance bandwidth, with a maximum isolation of −50 dBi at 30 GHz. Additionally, the inter-element isolation was drastically enhanced, with over > −25 dB observed between elements 1 and 2 and elements 1 and 4. The decrease in mutual coupling and improvement in isolation validated the effectiveness of the proposed decoupling concept and the theoretical analysis.

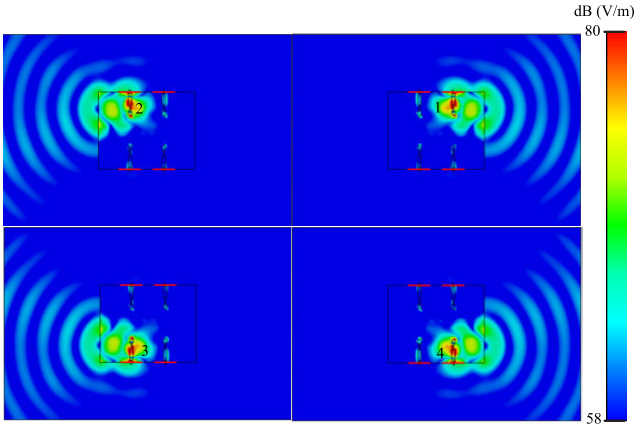

FIGURE 10. Electric field distribution of all four elements at 28 GHz.

The electric field and surface current distributions for the MIMO antenna with and without FSS when port one is active are displayed in Fig. 9. It is evident that the elements without the FSS structure are closely coupled, causing the electric field of port one to further disturb the field of port four. As previously discussed, the mutual coupling between these two ports is greater and is reduced by the insertion of the FSS, thereby improving the generation of electric fields in one direction. The current distribution reveals that the surface

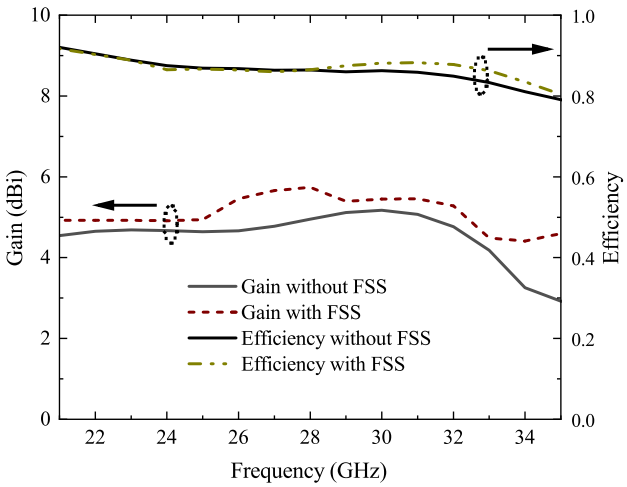

FIGURE 11. Simulated gain and efficiency with and without FSS.

current is predominantly concentrated on the inner edge of the exponential tapering structure, and is more concentrated in the presence of the FSS structure. Fig. 10 shows the electric field distribution for all ports, demonstrating that the MIMO antenna radiates in an end-fire pattern with minimal impact on nearby antenna elements. The gain and efficiency of the proposed MIMO antenna are slightly affected by the inclusion of the FSS, as shown in Fig. 11. The results show that adding FSS results in an increase in gain, with a peak gain of 5.73 dBi at 28 GHz observed. Additionally, the FSS structure leads to a small improvement in efficiency, with maximum efficiencies exceeding 86% and 87% at 28 GHz and 30 GHz, respectively.

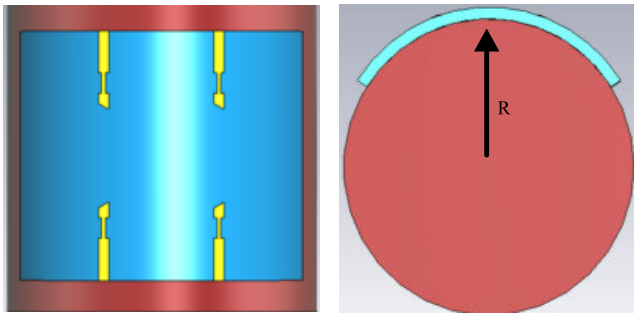

FIGURE 12. Bending of MIMO antenna on cylinder: (a) front (b) side view showing radius R.

III. RESULTS AND DISCUSSIONS OF MIMO ANTENNA FOR WBAN

A. CONFORMABILITY ANALYSIS

Conformability analysis of the MIMO antenna is essential for wearable device applications because the antennas can be affected by the different curvature of the body when placed on parts such as the hand or leg. To assess this, the antenna performance was tested when bent along different radii R

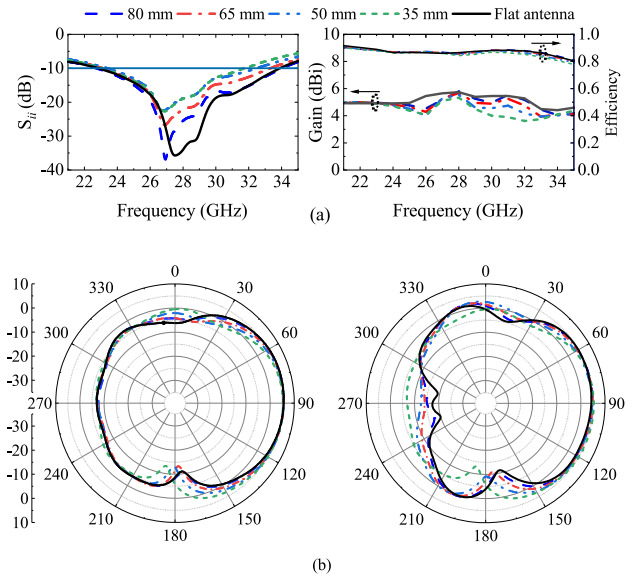

FIGURE 13. Bending analysis at different scenarios: (a) reflection coefficients (S_{11}, S_{44}), gain, and efficiency (b) normalized E-plane radiation pattern at 28 GHz (left) and 30 GHz (right).

(80 mm, 65 mm, 50 mm, and 35 mm) on a cylindrical model shaping the arm and leg regions, as shown in Fig. 12. The MIMO antenna S-parameters and efficiency during bending conditions are shown in Fig. 13(a), and it can be inferred that as the bending becomes more pronounced, the frequency shifts slightly towards lower frequencies. However, the resonant frequency still covers most frequencies, particularly 28 GHz and 30 GHz, respectively. This shift to lower frequencies is expected because the current path on the radiating patch elongates owing to the bending in both directions. Furthermore, constant efficiency was observed in all-bending scenarios of the proposed MIMO antenna. Fig. 13(b) presents the simulated radiation patterns of the E-plane at frequencies of 28 GHz and 30 GHz for various bending conditions, indicating a minimal difference between the flat and bent antennas in terms of their radiation characteristics. The consistent efficiency and far-field radiation characteristics of the MIMO antenna when in a bent state suggest that it is not highly susceptible to deformation.

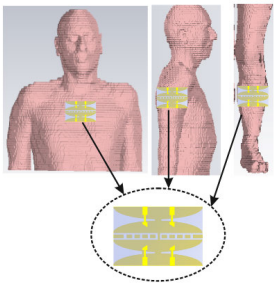

FIGURE 14. MIMO antenna on the chest, arm, and leg of the Gustav human body model.

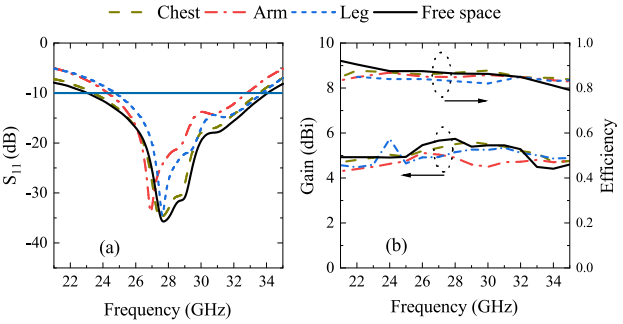

FIGURE 15. Comparison of MIMO antenna placed in free space and on the Gustav human body model: (a) reflection coefficients (b) gain and efficiency.

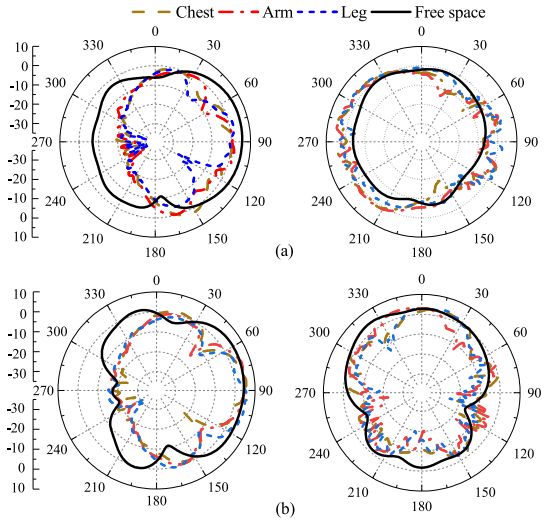

FIGURE 16. Comparison of the E-plane (left) and H-plane (right) radiation patterns on the body and in free space: (a) 28 GHz, and (b) 30 GHz.

TABLE 2. Antenna performance comparison on the body and in free space.

Antenna Position	Impedance B.W (GHz)	Peak Gain (dBi)	Efficiency
Free space	22.97 - 33.91	5.73	0.87
Chest	23.12 - 33.86	5.61	0.87
Arm	24.30 - 33.79	5.25	0.87
Leg	24.60 - 33.85	5.13	0.86

B. ANTENNA ON-BODY ANALYSIS

This section examines the antenna's S-parameters, gain, efficiency, and radiation patterns when placed in CST Studio Suite Gustav human model, as shown in Fig. 14. The MIMO antenna was placed on different anatomical regions of the voxel body (chest, arm, and leg) at a distance of 4.50 mm from the skin. This approach provides a practical and comfortable solution for various wearable devices. The thickness of the clothing typically ranges from 1 mm to 6 mm. If the clothing surpasses this thickness, it may adversely affect the antenna performance and imitate the performance of an off-body

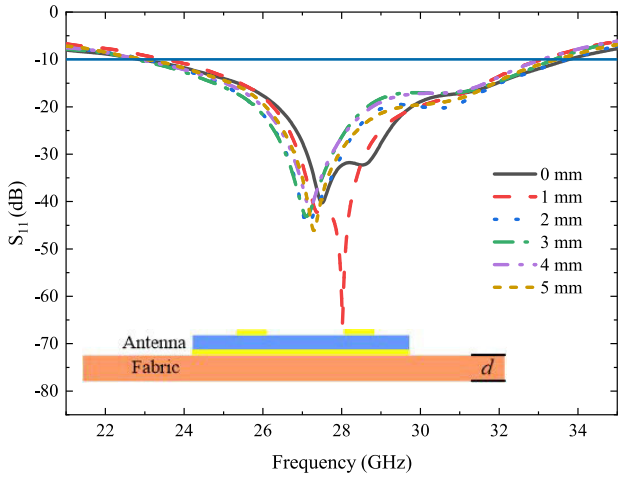

FIGURE 17. Reflection coefficient of the MIMO antenna (side view) in response to different thicknesses of the denim fabric material.

scenario owing to the existence of an appreciable amount of free space beneath the ground plane. Fig. 15 compares the simulated reflection coefficients, gain, and efficiency for both on-body and free space scenarios. As shown in Fig. 15(a), the impedance bandwidth of the MIMO antenna exhibits slight variations, depending on its placement in the human body. These variations may be attributed to alterations in the curvature of the regions on which the antenna is placed, namely, the arm and leg, which affect surface current flow. A nearly flat curvature of the chest results in smaller changes. As shown in Fig. 15(b), there are minor variations in the gain and efficiency compared to the free space scenario. However, the far-field characteristics of the antenna remained relatively steady for different placements on the human body, as shown in Fig 16. The small instability of radiation patterns in the leg and arm regions is clearly apparent, as reflected by the slightly shifted reflection coefficient (Fig. 15). This instability can be attributed to the non-flat surfaces of these regions. Despite this, the radiation pattern remains consistent with the endfire configuration. Table 2 presents a comparison of the changes in impedance bandwidth, peak gain, and efficiency for free space and on-body conditions.

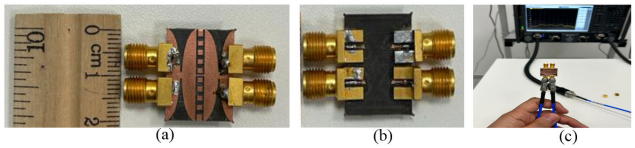

FIGURE 18. Fabricated prototype of MIMO antenna: (a) bottom (b) top, and (c) measurement using VNA.

C. IMPACT OF THE FABRIC ON THE MIMO ANTENNA

Integrating fabrics and MIMO antennas in close proximity poses challenges owing to the impact of fabrics on the antenna performance. Fabrics can weaken signals, cause signal scattering and reflection, alter the antenna impedance, and introduce unwanted coupling between multiple antennas in MIMO systems. The specific impact depends on the fabric dielectric properties and operating frequency of the fabric. It is essential to consider these factors during the design and deployment, particularly for wearable applications, to ensure optimal MIMO antenna performance. Denim, a commonly used fabric, has a permittivity of 1.79 from 24 GHz to 30 GHz [42]. To examine this, a model was designed to place the denim material below the designed MIMO antenna with different thicknesses (d). The reflection coefficient of the antenna was examined for various thicknesses. The findings, illustrated in Fig. 17, reveal that the performance of the antenna was not significantly affected. While a slight alteration in the bandwidth was observed with a 1 mm thickness, the effect diminished as the thickness increased, and the antenna approached the free space condition at approximately 5 mm. Although the effect was minimal under all conditions, the common thickness of the daily used denim material is up to 5 mm, making this thickness an optimal choice for placing the MIMO antenna. The antenna placement of 4.50 mm above the body during measurements in this work include the thickness of wearing clothing material.

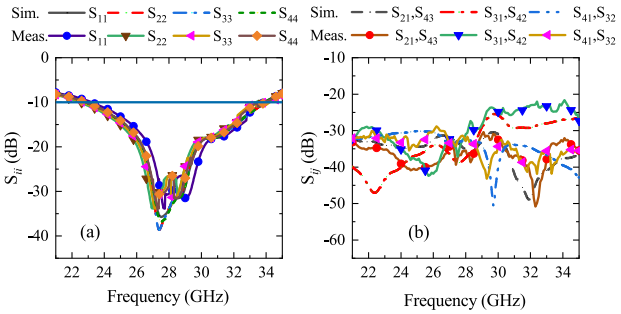

FIGURE 19. Comparison of simulated and measured S-parameters: (a) reflection coefficients, and (b) transmission coefficients.

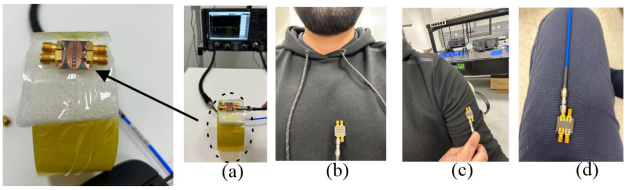

FIGURE 20. Bending and on-body measurements: (a) bending on tape (b) on chest, and (c) arm (d) leg.

D. EXPERIMENTAL VALIDATION

Fig. 18 showcases the fabricated prototype of the proposed MIMO antenna and its corresponding measurement using the Keysight network analyzer (PNA-X, N5247B). The S-parameter results for all four elements of the MIMO antenna under flat conditions and in free space are illustrated in Fig. 19. The measured outcomes indicate that the antenna's performance aligns with the simulated data, exhibiting an

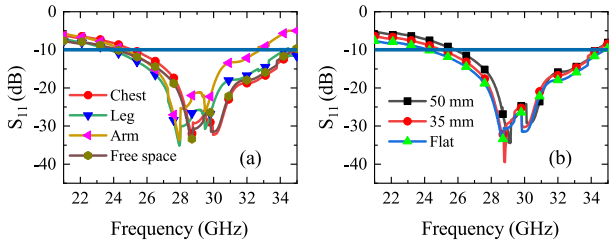

FIGURE 21. Measured reflection coefficients of the MIMO antenna: (a) on the body and free space, and (b) during bending.

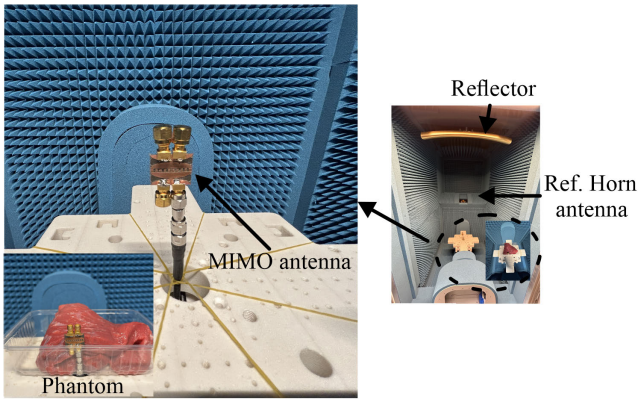

FIGURE 22. MIMO antenna and phantom in the anechoic chamber.

impedance bandwidth surpassing 10 GHz and transmission coefficients between each port exceeding −20 dB.

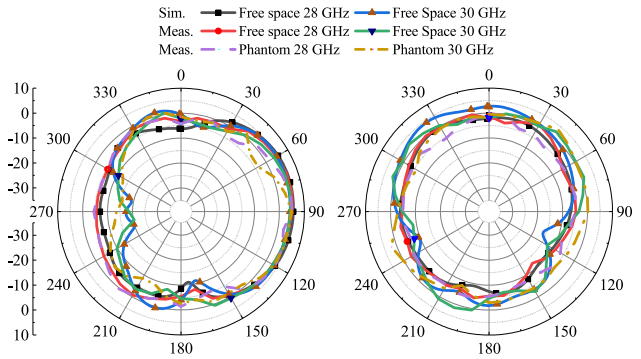

FIGURE 23. Simulated and measured radiation patterns of MIMO antenna: E-plane (left), and H-plane (right).

To evaluate the effects of antenna bending on its performance, the antenna was placed on foam layers of 35 mm and 50 mm in thickness, with relative permittivity of 1, which mimic free space. The antenna was also positioned on curved adhesive tape, as shown in Fig. 20(a), and the results were recorded in Fig. 21. Additionally, on-body measurements were conducted at a height of 4.50 mm, including the presence of a cloth layer across the chest, arm, and leg parts of the human body, as shown in Figs. 20(b)-(d). The results in Figs. 21(a)-(b) show a comparison of the antenna measurement results when placed on the body and positioned in free space and when the MIMO antenna is bent. The placement of the MIMO antenna on the arm and leg resulted in a slight reduction in the impedance bandwidth. For instance, the impedance bandwidth in free space was 10.94 GHz, which was reduced to 9.49 GHz and 9.25 GHz in the arm and leg regions. This change may be attributed to the different curvatures between the human arm and leg and the chest, with the latter exhibiting a relatively flatter surface.

The gain transfer technique was used to measure the gain of the proposed MIMO antenna. This approach is based on the principle of reciprocity and assesses antenna performance by measuring the power received from a reference antenna that has been calibrated at various angles. The gain of the receiving antenna can be determined by measuring the power received by the calibrated reference antenna during transmission. The gain measurements were conducted in a Rhodes & Schwarz RS®ATS1800C 5G anechoic chamber to ensure precision, as shown in Fig. 22. First, antenna-only measurements were performed, followed by the measurement of the on-body gain using a phantom (meat) to mimic the human body. The measured results for the E-plane and H-plane radiation patterns were compared with those of the simulations, as shown in Fig. 23. These results indicate a significant correlation between the simulated and measured data for end-fire radiation patterns. However, variations were observed during the phantom measurements, which can be attributed to the limitations in the fabrication and testing environments. Additionally, the measured results of gain and efficiency are provided for the antenna only and when placed on the phantom in Fig. 24. It is essential for the antenna to exhibit a consistent gain and efficiency when placed on the body to ensure reliable performance. The proposed antenna design offers consistent gain and efficiency throughout its impedance bandwidth, making it a promising choice for on-body mm-wave band WBAN applications.

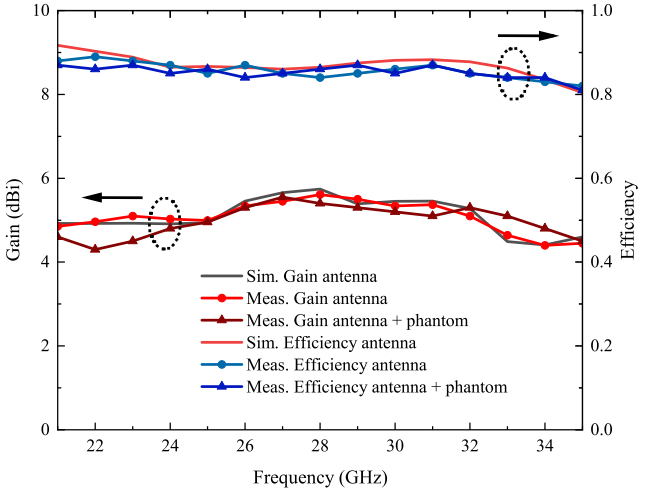

FIGURE 24. Simulated and measured gain and efficiency of the MIMO antenna.

IV. MIMO DIVERSITY PERFORMANCE ANALYSIS

This section analyzes the performance of the proposed MIMO antenna through an assessment of the diversity param-

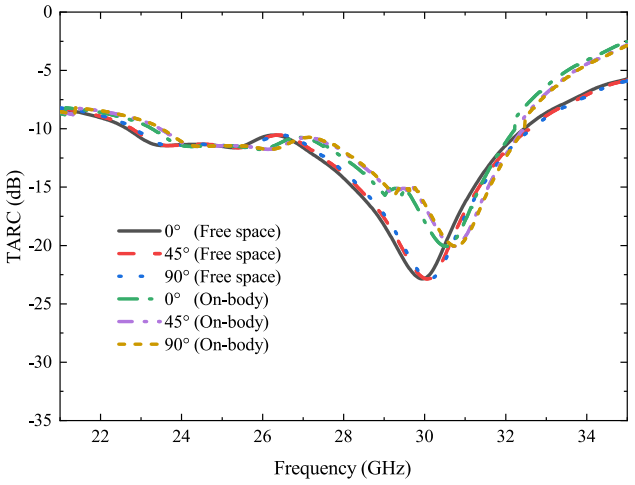

FIGURE 25. TARC of the MIMO antenna in free space and on the body.

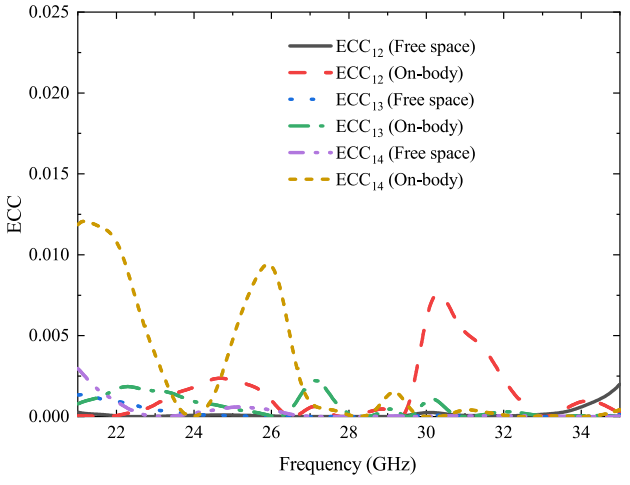

FIGURE 26. ECC of the MIMO antenna in free space and on the body.

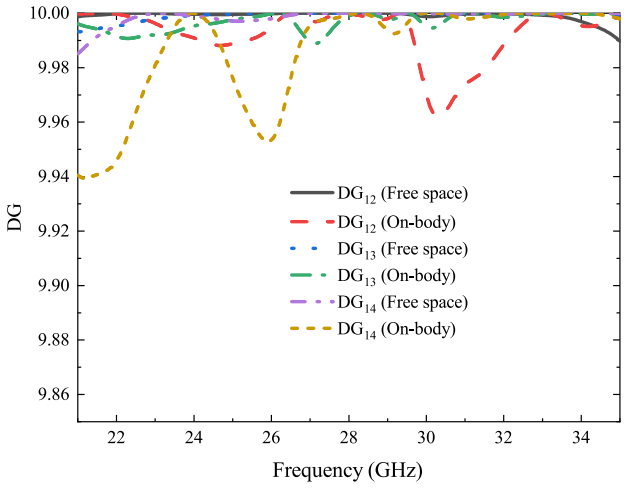

FIGURE 27. DG of the MIMO antenna in free space and on the body.

eters, including the total active reflection coefficient (TARC), envelope correlation coefficient (ECC), and diversity gain (DG). The methods for investigating and determining the MIMO diversity parameters are thoroughly explained in [43] and [44].

A. TARC ANALYSIS

The TARC parameter evaluates the effect of signal phase fluctuations on the reflection parameters of each antenna in a MIMO system. In other words, TARC is the ratio of the square root of the total reflected power to the square root of the total incident power in a MIMO antenna. The TARC parameter for the designed four-port MIMO antenna is mathematically formulated by utilizing equations 7-11 [44].

$$TARC = \frac{\sqrt{|S_1|^2 + |S_2|^2 + |S_3|^2 + |S_4|^2}}{\sqrt{4}} \tag{7}$$

where

$$S_1 = S_{11} + S_{12}e^{j\theta} + S_{13}e^{j\theta_1} + S_{14}e^{j\theta_2} \tag{8}$$
$$S_2 = S_{21} + S_{22}e^{j\theta} + S_{23}e^{j\theta_1} + S_{24}e^{j\theta_2} \tag{9}$$
$$S_3 = S_{31} + S_{32}e^{j\theta} + S_{33}e^{j\theta_1} + S_{34}e^{j\theta_2} \tag{10}$$
$$S_4 = S_{41} + S_{42}e^{j\theta} + S_{43}e^{j\theta_1} + S_{44}e^{j\theta_2} \tag{11}$$

Here θ, θ_1, and θ_2 are the input phase differences between the excitation ports. The TARC values for the proposed MIMO antenna for various input phases, both in free space and on the body, are given in Fig. 25. The findings demonstrate that the TARC values exceed -10 dB across a significant portion of the impedance bandwidth. Low TARC values imply that the MIMO antenna system can effectively transmit and receive signals without significant losses resulting from different phase varied input signals.

B. ECC AND DG ANALYSIS

The ECC quantifies the degree of correlation between radiating antenna elements and the extent to which their radiation patterns mutually influence one another during simultaneous operation. To achieve an ideal uncorrelated diversity performance, the ECC must be reduced to zero but a value below 0.5 is acceptable in practical applications. In this study, an ECC analysis was performed using far-field radiation patterns. ECC values for the m^{th} and n^{th} antenna elements are calculated using equations 12-14 [44].

$$ECC(m,n) = \frac{\left(\int_0^{2\pi}\int_0^{\pi}\left\{XPR.E_{\theta_m}E^*_{\theta_n}P_\theta + E_{\phi_m}E^*_{\phi_n}P_\phi\right\}d\Omega\right)^2}{\int_0^{2\pi}\int_0^{\pi}\left\{XPR.E_{\theta_m}E^*_{\theta_m}P_\theta + E_{\phi_m}E^*_{\phi_m}P_\phi\right\}d\Omega} \times \int_0^{2\pi}\int_0^{\pi}\left\{XPR.E_{\theta_n}E^*_{\theta_n}P_\theta + E_{\phi_n}E^*_{\phi_n}P_\phi\right\}d\Omega \tag{12}$$

Here, XPR denotes the cross-polarization ratio of the propagation environment and can be defined as:

$$XPR = \frac{P_v}{P_h} = 1 \tag{13}$$

TABLE 3. Proposed antenna comparison with other reported works.

Ref. No	[27]	[37]	[48]	[49]	[50]	**This work**
Antenna type	Yagi−Uda	Rectangle patch	Microstrip patch	Circular patch	Microstrip patch	**Vivaldi**
Frequency band	mm-wave	mm-wave	ISM	mm-wave	mm-wave	**mm-wave**
Bandwidth (GHz)	0.9	0.80	2.80	0.001/0.01	14.00	**10.94**
Substrate layer	Single	Two	Single	Single	Single	**Single**
Dimensions	14.96×17.45	15.06×19.04	14.96×17.45	60×60	28×8	**16×20**
Gain (dBi)	5.20	6.00	7.50	−0.82/2.83	8.86	**5.65**
Efficiency	–	0.80	0.80	0.60	0.65	**0.86**
Bending analysis	Yes	Yes	No	Yes	Yes	**Yes**
Antenna elements	NA	2	NA	NA	Array 2x2	**4**

–; not given, NA: not applicable

In addition, the diversity performance of the MIMO antenna in terms of the transmitted power can be represented as the DG:

$$DG = 10\sqrt{1 - (ECC)^2} \tag{14}$$

Figs. 26 and 27 show the ECC and DG parameters of all the elements of the MIMO antenna in free space and on the body. As can be observed, the ECC values are well below the standard of 0.5 and are approaching zero throughout the impedance bandwidth. Similarly, as shown in Fig. 27, the MIMO antenna has exceptional DG values exceeding 9.95 dB, which are close to the standard threshold of 10 dB across the impedance bandwidth.

V. SAR ANALYSIS

The safety evaluation of wearable devices depends on the absorption of electromagnetic radiation by biological tissues, which is measured as the SAR. Owing to the shorter wavelengths of mm-wave frequencies, the penetration depth is limited to the skin region only. The Federal Communications Commission (FCC) and the International Commission on Non-Ionizing Radiation Protection (ICNIRP) have established SAR standards for frequencies below 6 GHz, with values of 1.6 W/kg and 2 W/kg, respectively [45], no specific SAR standards exist for mm-wave frequencies yet. Although the concept of spatial power density has been proposed as a potential alternative to SAR, it is yet to be fully developed, and challenges persist [46]. As a result, current standards were applied to assess MIMO antenna.

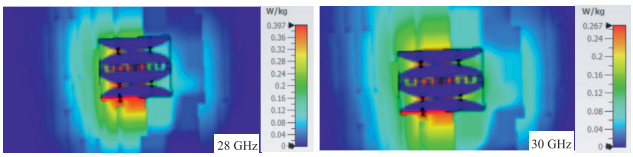

FIGURE 28. SAR distribution of the MIMO antenna.

The antenna was placed at a distance of 4.50 mm above the arm region of the Gustav voxel model in CST Studio Suite. The SAR values were assessed in with the stringent requirements outlined in IEEE C95.1-1999 for 1g of tissue, which impose a maximum average SAR limit of 1.6 W/kg. Because the input power value for wearable devices is 17 dBm (50 mW) [47], the same power was selected while simulating for SAR. The distribution of the SAR at frequencies of 28 GHz and 30 GHz is shown in Fig. 28. Maximum electromagnetic radiation absorption was observed immediately below the MIMO antenna. The SAR values for both frequencies were 0.397 W/kg and 0.267 W/kg, respectively. These values are well below the standard limit of 1.6 W/kg. Based on these findings, it can be concluded that the proposed MIMO design is safe for wearable WBAN applications.

VI. COMPARATIVE ANALYSIS

A compassion analysis is conducted to asses the suggested design antenna with previously reported works. The noteworthy characteristics of the proposed antenna include its four elements in compact space, which supports MIMO communication on a single substrate layer. In addition, the antenna exhibits a broad bandwidth when directly attached to the human body and demonstrates excellent efficiency with a favorable end-fire radiation pattern. The significance of this antenna is its constant gain, efficiency, and high isolation which remains consistent over the entire impedance bandwidth. The low SAR threshold with exceptional gain, efficiency, and bandwidth of the proposed four-port MIMO antenna make it promising solution for on and off-body communication in wearable devices. Table 3 lists the proposed comparision with other reported work.

VII. CONCLUSION

A low-profile Vivaldi antenna for wearable millimeter-wave applications was reported, operating from 23 − 34 GHz with a 36.44% fractional bandwidth and inter-element isolation of less than −20 dB. The antenna was tested on the Gustav model and various parts of the human body, including the chest, hand, and leg, including bending analysis. The chest

surface had a minimal effect on the bandwidth while the arm and leg had the most degradation owing to the curved tissue surface, which reduces impedance bandwidth. The antenna's performance was assessed with diversity performance such as TARC (< -10 dB), ECC (< 0.24), and DG (> 9.95 dB), as well as consistent gain (> 5.65 dBi) and efficiency (> 0.86) over the entire bandwidth. The SAR analysis showed acceptable 0.397 and 0.267 (W/kg) levels at 28 GHz and 30 GHz, respectively. The small size (16×20 mm^2) and its compatibility with the human body, regardless of bending, make the proposed design suitable for wearable WBAN applications.

REFERENCES

[1] B. Cornet, H. Fang, H. Ngo, E. W. Boyer, and H. Wang, "An overview of wireless body area networks for mobile health applications," *IEEE Netw.*, vol. 36, no. 1, pp. 76–82, Jan. 2022.

[2] M. Zhumayeva, K. Dautov, M. Hashmi, and G. Nauryzbayev, "Wireless energy and information transfer in WBAN: A comprehensive state-of-the-art review," *Alexandria Eng. J.*, vol. 85, pp. 261–285, Dec. 2023.

[3] A. Kiourti, A. M. Abbosh, M. Athanasiou, T. Björninen, A. Eid, C. Furse, K. Ito, G. Lazzi, M. Manoufali, M. Pastorino, M. M. Tentzeris, K. Tisdale, E. Topsakal, L. Ukkonen, W. G. Whittow, H. Zhang, and K. S. Nikita, "Next-generation healthcare: Enabling technologies for emerging bioelectromagnetics applications," *IEEE Open J. Antennas Propag.*, vol. 3, pp. 363–390, 2022.

[4] N. Bradai, L. Chaari Fourati, and L. Kamoun, "WBAN data scheduling and aggregation under WBAN/WLAN healthcare network," *Ad Hoc Netw.*, vol. 25, pp. 251–262, Feb. 2015.

[5] K. Zhang, Z. H. Jiang, W. Hong, and D. H. Werner, "A low-profile and wideband triple-mode antenna for wireless body area network concurrent on-/off-body communications," *IEEE Trans. Antennas Propag.*, vol. 68, no. 3, pp. 1982–1994, Mar. 2020.

[6] D. Rano and M. Hashmi, "Extremely compact EBG-backed antenna for smartwatch applications in medical body area network," *IET Microw., Antennas Propag.*, vol. 13, no. 7, pp. 1031–1040, Jun. 2019.

[7] P. K. Sharma, N. Gupta, and P. I. Dankov, "Characterization of polydimethylsiloxane (PDMS) as a wearable antenna substrate using resonance and planar structure methods," *AEU-Int. J. Electron. Commun.*, vol. 127, Dec. 2020, Art. no. 153455.

[8] R. B. V. B. Simorangkir, Y. Yang, K. P. Esselle, and B. A. Zeb, "A method to realize robust flexible electronically tunable antennas using polymer-embedded conductive fabric," *IEEE Trans. Antennas Propag.*, vol. 66, no. 1, pp. 50–58, Jan. 2018.

[9] A. Arif, M. Zubair, M. Ali, M. U. Khan, and M. Q. Mehmood, "A compact, low-profile fractal antenna for wearable on-body WBAN applications," *IEEE Antennas Wireless Propag. Lett.*, vol. 18, pp. 981–985, 2019.

[10] U. Ali, S. Ullah, B. Kamal, L. Matekovits, and A. Altaf, "Design, analysis and applications of wearable antennas: A review," *IEEE Access*, vol. 11, pp. 14458–14486, 2023.

[11] D. Rano and M. Hashmi, "Design and analysis of wearable patch antenna array for MBAN applications," in *Proc. 22nd Nat. Conf. Commun. (NCC)*, Guwahati, India, Mar. 2016, pp. 1–6.

[12] M. M. H. Mahfuz, M. R. Islam, C.-W. Park, E. A. A. Elsheikh, F. M. Suliman, M. H. Habaebi, N. A. Malek, and N. Sakib, "Wearable textile patch antenna: Challenges and future directions," *IEEE Access*, vol. 10, pp. 38406–38427, 2022.

[13] H. Li, J. Du, X.-X. Yang, and S. Gao, "Low-profile all-textile multiband microstrip circular patch antenna for WBAN applications," *IEEE Antennas Wireless Propag. Lett.*, vol. 21, pp. 779–783, 2022.

[14] V. Kumar and B. Gupta, "On-body measurements of SS-UWB patch antenna for WBAN applications," *AEU - Int. J. Electron. Commun.*, vol. 70, no. 5, pp. 668–675, May 2016.

[15] P. B. Samal, P. J. Soh, and Z. Zakaria, "Compact microstrip-based textile antenna for 802.15.6 WBAN-UWB with full ground plane," *Int. J. Antennas Propag.*, vol. 2019, pp. 1–12, Mar. 2019.

[16] Y. Li, L. Yang, M. Gao, X. Zhao, and X. Zhang, "A study of a one-turn circular patch antenna array and the influence of the human body on the characteristics of the antenna," *Ad Hoc Netw.*, vol. 99, Mar. 2020, Art. no. 102059.

[17] R. Zhang, J. Liu, Y. Wang, Z. Luo, B. Zhang, and J. Duan, "Flexible wearable composite antennas for global wireless communication systems," *Sensors*, vol. 21, no. 18, p. 6083, Sep. 2021, doi: 10.3390/s21186083.

[18] M. El Atrash, M. A. Abdalla, and H. M. Elhennawy, "A wearable dual-band low profile high gain low SAR antenna AMC-backed for WBAN applications," *IEEE Trans. Antennas Propag.*, vol. 67, no. 10, pp. 6378–6388, Oct. 2019.

[19] R. Joshi, E. F. N. M. Hussin, P. J. Soh, M. F. Jamlos, H. Lago, A. A. Al-Hadi, and S. K. Podilchak, "Dual-band, dual-sense textile antenna with AMC backing for localization using GPS and WBAN/WLAN," *IEEE Access*, vol. 8, pp. 89468–89478, 2020.

[20] Y. B. Chaouche, M. Nedil, I. B. Mabrouk, and O. M. Ramahi, "A wearable circularly polarized antenna backed by AMC reflector for WBAN communications," *IEEE Access*, vol. 10, pp. 12838–12852, 2022.

[21] U. Ali, S. Ullah, A. Basir, B. Kamal, L. Matekovits, and H. Yoo, "Design and SAR analysis of AMC-based fabric antenna for body-centric communication," *IEEE Access*, vol. 11, pp. 73894–73911, 2023.

[22] M. Bose, A. Kundu, A. Sarkhel, and U. Chakraborty, "A review of design challenges of metamaterial-inspired body-worn antennas," *Adv. Microw. Eng.*, pp. 115–144, Sep. 2023.

[23] C. Constantinescu, C. Pacurar, A. Giurgiuman, C. Munteanu, S. Andreica, and M. Gliga, "High gain improved planar Yagi uda antenna for 2.4 GHz applications and its influence on human tissues," *Appl. Sci.*, vol. 13, no. 11, p. 6678, May 2023.

[24] A. Kafizov, M. Hashmi, D. Rano, and D. Kupreyev, "End-fire Yagi antenna with DGS for WBAN applications," in *Proc. 8th Asia–Pacific Conf. Antennas Propag. (APCAP)*, Aug. 2019, pp. 426–427.

[25] Z. Iman, A. Shungeyev, D. Rano, and M. Hashmi, "A planar end-fire antenna for wireless body area network," in *Proc. Int. Workshop Antenna Technol. (iWAT)*, Feb. 2020, pp. 1–3.

[26] S. Vuppala, Y. J. Tolossa, G. Kaddoum, and G. Abreu, "On the physical layer security analysis of hybrid millimeter wave networks," *IEEE Trans. Commun.*, vol. 66, no. 3, pp. 1139–1152, Mar. 2018.

[27] A. Guraliuc, N. Chahat, C. Leduc, M. Zhadobov, and R. Sauleau, "End-fire antenna for BAN at 60 GHz: Impact of bending, on-body performances, and study of an on to off-body scenario," *Electronics*, vol. 3, no. 2, pp. 221–233, Apr. 2014.

[28] M. I. Magray, S.-W. Su, and J.-H. Tarng, "Differential-fed, dual-aperture based, quasi-end-fire 5G mmWave antenna-in-package design," *IEEE Access*, vol. 10, pp. 89091–89100, 2022.

[29] N. Chahat, M. Zhadobov, L. Le Coq, and R. Sauleau, "Wearable endfire textile antenna for on-body communications at 60 GHz," *IEEE Antennas Wireless Propag. Lett.*, vol. 11, pp. 799–802, 2012.

[30] N. Chahat, M. Zhadobov, S. A. Muhammad, L. Le Coq, and R. Sauleau, "60-GHz textile antenna array for body-centric communications," *IEEE Trans. Antennas Propag.*, vol. 61, no. 4, pp. 1816–1824, Apr. 2013.

[31] M. Wagih, G. S. Hilton, A. S. Weddell, and S. Beeby, "Broadband millimeter-wave textile-based flexible rectenna for wearable energy harvesting," *IEEE Trans. Microw. Theory Techn.*, vol. 68, no. 11, pp. 4960–4972, Nov. 2020.

[32] V. K. Jhunjhunwala, T. Ali, P. Kumar, P. Kumar, P. Kumar, S. Shrivastava, and A. A. Bhagwat, "Flexible UWB and MIMO antennas for wireless body area network: A review," *Sensors*, vol. 22, no. 23, p. 9549, Dec. 2022.

[33] Q. Liu, K. G. Mkongwa, and C. Zhang, "Performance issues in wireless body area networks for the healthcare application: A survey and future prospects," *Social Netw. Appl. Sci.*, vol. 3, no. 2, Feb. 2021.

[34] S. Wang, Y. Ji, D. Gibbins, and X. Yin, "Impact of dynamic wideband MIMO body channel characteristics on healthcare rehabilitation of walking," *IEEE Antennas Wireless Propag. Lett.*, vol. 16, pp. 505–508, 2017.

[35] L. Wang, Z. Du, H. Yang, R. Ma, Y. Zhao, X. Cui, and X. Xi, "Compact UWB MIMO antenna with high isolation using fence-type decoupling structure," *IEEE Antennas Wireless Propag. Lett.*, vol. 18, pp. 1641–1645, 2019.

[36] C. X. Mao, Y. Zhou, Y. Wu, H. Soewardiman, D. H. Werner, and J. S. Jur, "Low-profile strip-loaded textile antenna with enhanced bandwidth and isolation for full-duplex wearable applications," *IEEE Trans. Antennas Propag.*, vol. 68, no. 9, pp. 6527–6537, Sep. 2020.

[37] A. Iqbal, A. Basir, A. Smida, N. K. Mallat, I. Elfergani, J. Rodriguez, and S. Kim, "Electromagnetic bandgap backed millimeter-wave MIMO antenna for wearable applications," *IEEE Access*, vol. 7, pp. 111135–111144, 2019.
[38] X. Shi, Y. Cao, Y. Hu, X. Luo, H. Yang, and L. H. Ye, "A high-gain antipodal Vivaldi antenna with director and metamaterial at 1–28 GHz," *IEEE Antennas Wireless Propag. Lett.*, vol. 20, pp. 2432–2436, 2021.
[39] Z. Wang, C. Li, and Y. Yin, "A meta-surface antenna array decoupling (MAAD) design to improve the isolation performance in a MIMO system," *IEEE Access*, vol. 8, pp. 61797–61805, 2020.
[40] S. Guruswamy, R. Chinniah, and K. Thangavelu, "A printed compact UWB Vivaldi antenna with hemi cylindrical slots and directors for microwave imaging applications," *AEU-Int. J. Electron. Commun.*, vol. 110, Oct. 2019, Art. no. 152870.
[41] Z. Szabó, G.-H. Park, R. Hedge, and E.-P. Li, "A unique extraction of metamaterial parameters based on Kramers–Kronig relationship," *IEEE Trans. Microw. Theory Techn.*, vol. 58, no. 10, pp. 2646–2653, Oct. 2010.
[42] S. W. Harmer, N. Rezgui, N. Bowring, Z. Luklinska, and G. Ren, "Determination of the complex permittivity of textiles and leather in the 14–40 GHz millimetre-wave band using a free-wave transmittance only method," *IET Microw., Antennas Propag.*, vol. 2, no. 6, pp. 606–614, Sep. 2008.
[43] K. S. Sultan and H. H. Abdullah, "Planar UWB MIMO-diversity antenna with dual notch characteristics," *Prog. Electromagn. Res. C*, vol. 93, pp. 119–129, 2019.
[44] R. N. Tiwari, P. Singh, B. K. Kanaujia, and K. Srivastava, "Neutralization technique based two and four port high isolation MIMO antennas for UWB communication," *AEU-Int. J. Electron. Commun.*, vol. 110, Oct. 2019, Art. no. 152828.
[45] G. Ziegelberger, R. Croft, M. Feychting, A. C. Green, A. Hirata, G. d'Inzeo, K. Jokela, S. Loughran, C. Marino, S. Miller, and G. Oftedal, "Guidelines for limiting exposure to electromagnetic fields (100 kHz to 300 GHz)," *Health Phys.*, vol. 118, no. 5, pp. 483–524, 2020.
[46] M. Redmayne and D. R. Maisch, "ICNIRP guidelines' exposure assessment method for 5G millimetre wave radiation may trigger adverse effects," *Int. J. Environ. Res. Public Health*, vol. 20, no. 7, p. 5267, Mar. 2023.
[47] I. Gil, R. Seager, and R. Fernández-García, "Embroidered metamaterial antenna for optimized performance on wearable applications," *Phys. Status Solidi (A)*, vol. 215, no. 21, Aug. 2018, Art. no. 1800377.
[48] P. Njogu, B. Sanz-Izquierdo, A. Elibiary, S. Y. Jun, Z. Chen, and D. Bird, "3D printed fingernail antennas for 5G applications," *IEEE Access*, vol. 8, pp. 228711–228719, 2020.
[49] D. Wen, Y. Hao, M. O. Munoz, H. Wang, and H. Zhou, "A compact and low-profile MIMO antenna using a miniature circular high-impedance surface for wearable applications," *IEEE Trans. Antennas Propag.*, vol. 66, no. 1, pp. 96–104, Jan. 2018.
[50] S. F. Jilani, M. O. Munoz, Q. H. Abbasi, and A. Alomainy, "Millimeter-wave liquid crystal polymer based conformal antenna array for 5G applications," *IEEE Antennas Wireless Propag. Lett.*, vol. 18, pp. 84–88, 2019.

JAWAD AHMAD (Student Member, IEEE) received the B.S. and M.S. degrees in electronics and electrical engineering from the International Islamic University Islamabad (IIUI), Pakistan, in 2017 and 2020, respectively. He is currently pursuing the Ph.D. degree with the Department of Electrical and Computer Engineering, Nazarbayev University, Astana, Kazakhstan. His research is focused on radio frequency (RF) and microwave engineering, with a particular emphasis on the design of 5G MIMO antennas and metamaterials-inspired wearable antennas for biomedical applications.

MOHAMMAD HASHMI (Senior Member, IEEE) received the B.Tech. degree from Aligarh Muslim University, India, the M.S. degree from Darmstadt University of Technology, Germany, and the Ph.D. degree from Cardiff University, Cardiff, U.K. He has held research, engineering, and academic positions with the University of Calgary, Canada; Cardiff University; Thales Electronics GmbH, Germany; Philips Technology Center, Germany; and IIIT Delhi, India. He is currently an Associate Professor with Nazarbayev University, Kazakhstan. His research activities have led to one book, three U.S. patents (two pending), and over 300 journals and conference publications. His current research interests include the domain of advanced RF circuits for wireless applications (including wireless power transfer and energy harvesting), emerging RF circuits and applications, broadband linear and efficient power amplifiers for mobile and satellite applications, and high- and low-frequency instrumentation. He is an Associate Editor of *IEEE Microwave Magazine*.

AZAMAT BAKYTBEKOV received the Ph.D. degree from the Electrical Engineering Department, Integrated Microwaves Packaging Antennas and Circuit Technology (IMPACT) Research Group, King Abdullah University of Science and Technology (KAUST), Saudi Arabia. His research interests include antenna design, rectifier and matching circuit design, energy harvesting through ambient sources (RF, thermal, and solar), antenna design and communication systems for UAVs, 3-D printing and inkjet printing techniques, and integration and miniaturization techniques.

FRANCISCO FALCONE (Senior Member, IEEE) received the degree in telecommunication engineering and the Ph.D. degree in communication engineering from the Public University of Navarre (UPNA), Spain, in 1999 and 2005, respectively. From February 1999 to April 2000, he was a Microwave Commissioning Engineer with Siemens-Italtel, deploying microwave access systems. From May 2000 to December 2008, he was a Radio Access Engineer with Telefónica Móviles, performing radio network planning and optimization tasks in mobile network deployment. As a Co-Founding Member in January 2009, he has been the Director of Tafco Metawireless, a spin-off company from UPNA, until May 2009. He was an Assistant Lecturer with the Electrical and Electronic Engineering Department, UPNA, from February 2003 to May 2009. In June 2009, he become an Associate Professor with the EE Department, being the Department Head, from January 2012 to July 2018. From January 2018 to May 2018, he was a Visiting Professor with Kuwait College of Science and Technology, Kuwait. He is also affiliated with the Institute for Smart Cities (ISC), UPNA, which hosts around 140 researchers. He has over 500 contributions in indexed international journals, book chapters, and conference contributions. His research interests include computational electromagnetics applied to the analysis of complex electromagnetic scenarios, with a focus on the analysis, design, and implementation of heterogeneous wireless networks to enable context-aware environments. He is currently acting as the Head of the ICT Section. He received the CST 2003 and CST 2005 Best Paper Award; the Ph.D. Award from the Colegio Oficial de Ingenieros de Telecomunicación (COIT), in 2006; the Doctoral Award UPNA, in 2010; the first Juan Gomez Peñalver Research Award from the Royal Academy of Engineering of Spain, in 2010; the XII Talgo Innovation Award, in 2012; the IEEE 2014 Best Paper Award. in 2014,; the ECSA-3 Best Paper Award, in 2016; and the ECSA-4 Best Paper Award, in 2017.